



**HAL**  
open science

# Fourier-based schemes with modified Green operator for computing the electrical response of heterogeneous media with accurate local fields

François Willot, Bassam Abdallah, Yves-Patrick Pellegrini

► **To cite this version:**

François Willot, Bassam Abdallah, Yves-Patrick Pellegrini. Fourier-based schemes with modified Green operator for computing the electrical response of heterogeneous media with accurate local fields. 2013. hal-00840986v1

**HAL Id: hal-00840986**

**<https://hal.science/hal-00840986v1>**

Preprint submitted on 3 Jul 2013 (v1), last revised 21 Aug 2014 (v2)

**HAL** is a multi-disciplinary open access archive for the deposit and dissemination of scientific research documents, whether they are published or not. The documents may come from teaching and research institutions in France or abroad, or from public or private research centers.

L'archive ouverte pluridisciplinaire **HAL**, est destinée au dépôt et à la diffusion de documents scientifiques de niveau recherche, publiés ou non, émanant des établissements d'enseignement et de recherche français ou étrangers, des laboratoires publics ou privés.

# Fourier-based schemes with modified Green operator for computing the electrical response of heterogeneous media with accurate local fields

François Willot<sup>†1</sup>, Bassam Abdallah<sup>†</sup> and Yves-Patrick Pellegrini<sup>\*</sup>

<sup>†</sup> Mines ParisTech, Centre de Morphologie Mathématique, 35 rue Saint Honoré, 77305 Fontainebleau Cedex, France.

<sup>\*</sup> CEA, DAM, DIF, F-91297 Arpajon, France.

A modified Green operator is proposed as an improvement of Fourier-based numerical schemes commonly used for computing the electrical or thermal response of heterogeneous media. Contrary to other methods, the number of iterations necessary to achieve convergence tends to a finite value when the contrast of properties between the phases becomes infinite. Furthermore, it is shown that the method produces much more accurate local fields inside highly-conducting and quasi-insulating phases, as well as in the vicinity of the phases interfaces. These good properties stem from the discretization of Green’s function, which is consistent with the pixel grid while retaining the local nature of the operator that acts on the polarization field. Finally, a fast implementation of the “direct scheme” of Moulinec et al. (1994) that allows for parcimonious memory use is proposed.

Keywords: FFT methods; Numerical homogenization; Heterogeneous media; Electrical conductivity.

## 1. INTRODUCTION

In recent years, Fourier-based methods, originally introduced by Moulinec et al. [1], have become ubiquitous for computing numerically the properties of composite materials, with applications in domains ranging from linear elasticity [2], viscoplasticity [3], crack propagation [4] to thermal and electrical [5, 6], but also optical properties [7]. The success of the method resides in its ability to cope with arbitrarily complex and often very large microstructures, supplied as segmented images of real materials, e.g., multi-scale nano-composites [8], austenitic steel [9], granular media [5] or polycrystals [10–12]. This technique allows maps of the local fields to be computed in realistic microstructures. Such fields are representative of the material behavior if the resolution is small enough, and if the system size is large enough, compared with the typical length scale of the heterogeneities. Contrary to finite-element methods where matrix pre-conditioning often necessitates additional memory occupation, Fast-Fourier-Transform (FFT) methods are limited only by the amount of RAM or fast-access computer memory required to store the fields.

The use of an image and of its underlying equispaced grid however comes with drawbacks not seen in finite-element methods. First, FFT methods will ultimately be less efficient when dealing with highly porous media like foams, where voids need to be discretized. Second, interfaces are crudely rendered when using voxel grids, although smoothness can be somewhat recovered by introducing intermediate properties between the phases [13, 14]. This matter is most important for ideal microstructure models where interfaces are completely known; less so when dealing with experimental images where such information is usually absent. Third, the representation of the fields in terms of harmonic functions introduce oscillations around interfaces, which is akin to Gibbs’s phenomenon. High-frequency artifacts are conspicuous in many field maps where oscillations are visi-

ble. Fourth, the Fourier representation presupposes periodicity, i.e., the microstructure is seen as the elementary cell of an infinite, periodic medium. However, finite-size effects associated to periodic boundary conditions are generally smaller than that of uniform boundary conditions used in finite-element methods [15].

In the present work, use is made of an alternative discretization of the Green function leading to a revisit of previously developed FFT algorithms. Specifically, their performances in terms of accuracy and speed are investigated. Our paper is organized as follows: the numerical problem and FFT algorithms are presented in Secs. 2 and 3, respectively. An alternative discretization is introduced in Sec. 4. The accuracy of the local fields is investigated in Sec. 5 and the convergence properties of FFT schemes, using the modified and unmodified Green functions, are studied in Sec. 6. Finally, a specific implementation of the FFT method using the modified Green function is proposed in Sec. 7.

## 2. PROBLEM SETUP AND LIPPMANN-SCHWINGER’S EQUATION

This work investigates the numerical computation of the electrical field  $E_i(\mathbf{x})$  and current field  $J_i(\mathbf{x})$  ( $i = 1, \dots, d$ ), in a  $d$ -dimensional cubic domain  $\Omega = [-L/2, L/2]^d$  of width  $L$  for  $d = 2$  or  $3$ . The fields verify (chap. 2 in [16])

$$\partial_i J_i(\mathbf{x}) = 0, \quad E_i(\mathbf{x}) = -\partial_i \Phi(\mathbf{x}), \quad J_i(\mathbf{x}) = \sigma_{ij}(\mathbf{x}) E_j(\mathbf{x}), \quad (1)$$

where  $\Phi(\mathbf{x})$  is the electric potential and  $\sigma(\mathbf{x})$  is the local conductivity tensor of the material phase at point  $\mathbf{x}$ . Thereafter, for simplicity, all media are locally linear and isotropic so that  $\sigma_{ij} = \sigma \delta_{ij}$ , with  $\sigma(\mathbf{x})$  a scalar field. Only binary composite media are considered in this study, in which inclusions have variable conductivity  $\sigma_2$ , and where conventionally  $\sigma_1=1$  in the matrix. Edges of  $\Omega$  are aligned with Cartesian axis of unit vectors  $(\mathbf{e}_i)_{1 \leq i \leq d}$ . Periodic boundary condi-

<sup>1</sup>Corresponding author. E-mail: francois.willot@ensmp.fr

tions are employed, in the form

$$\mathbf{J}(\mathbf{x}) \cdot \mathbf{n} - \# \quad \Phi(\mathbf{x} + L\mathbf{e}_i) \equiv \Phi(\mathbf{x}) - \bar{E}_i L, \quad \mathbf{x}, \mathbf{x} + L\mathbf{e}_i \in \partial\Omega, \quad (2)$$

where  $-\#$  denotes anti-periodicity,  $\mathbf{n}$  is the outer normal along the boundary  $\partial\Omega$  of  $\Omega$  and  $\bar{\mathbf{E}}$  is the applied electric field. They ensure that the current flux and the electrical field verify Eq. (1) along the boundary  $\partial\Omega$  of the periodic medium. Note that  $\bar{\mathbf{E}}$  represents a macroscopic electric field so that  $\langle E_i(\mathbf{x}) \rangle = \bar{E}_i$ , where  $\langle \cdot \rangle$  is the volume average over  $\Omega$ .

All FFT methods proceed from Lippmann-Schwinger's equation ([16] p. 251)

$$E_i = \bar{E}_i - G_{ij}^0 * P_j, \quad P_j = J_j - \sigma^0 E_j, \quad (3)$$

where  $\sigma^0$  is an arbitrary reference conductivity,  $\mathbf{P}$  and  $\mathbb{G}^0$  are the associated polarization field and Green operator, respectively, and  $*$  is the convolution product. An equivalent "dual" formulation stems from writing the problem in terms of the electric current, as

$$J_i = \bar{J}_i - H_{ij}^0 * T_j, \quad T_j = E_j - \rho^0 J_j, \quad (4)$$

where  $\rho^0 = 1/\sigma^0$  is the reference resistivity and  $\bar{\mathbf{J}}$  is the prescribed macroscopic current. The Green operator associated to the governing equation for the current reads

$$H_{ij}^0(\mathbf{x}) = \sigma^0 \{ [\delta(\mathbf{x}) - 1] \delta_{ij} - \sigma^0 G_{ij}^0(\mathbf{x}) \}, \quad (5)$$

where  $\delta(\mathbf{x})$  is Dirac's distribution and  $\delta_{ij}$  is the Kronecker symbol. Thus, for all  $\mathbf{T}$ ,

$$H_{ij}^0 * T_j = \sigma^0 (T_i - \langle T_i \rangle_\Omega - \sigma^0 G_{ij}^0 * T_j). \quad (6)$$

In particular  $\langle H_{ij}^0 * T_j \rangle = \langle G_{ij}^0 * T_j \rangle = 0$  and Eq. (4) enforces  $\bar{\mathbf{J}} = \langle \mathbf{J} \rangle$ . The FFT algorithms considered in this paper rest on evaluating the convolution product in Eqs. (3) or (4) in the Fourier domain, using FFT libraries.

### 3. FFT METHODS

Although most of FFT methods have been introduced in the context of elasticity, their adaptation to conductivity problems is straightforward. Hereafter all FFT algorithms are formulated in this setting. Equation (3) is the basis of the simplest method, the "direct" scheme [1]. Iterations consist in applying:

$$\mathbf{E}^{k+1} = \bar{\mathbf{E}} - G^0 * [(\sigma - \sigma^0)\mathbf{E}^k] \quad (7)$$

where  $\mathbf{E}^k$  is the electrical field at iteration  $k$ .

Over time, refined FFT algorithms with faster convergence properties have been devised, notably the "accelerated" [17] and "augmented-Lagrangian" [18] schemes. Both algorithms can be encapsulated in the formula [19, 20]

$$\mathbf{E}^{k+1} = \mathbf{E}^k + \frac{\sigma^0 [\bar{\mathbf{E}} - \langle \mathbf{E}^k \rangle - \beta \mathbb{G}^0 * (\sigma \mathbf{E}^k)] - \mathbb{H}^0 * \mathbf{E}^k}{\alpha(\sigma + \beta\sigma^0)} \quad (8)$$

where  $\alpha = \beta = 1$  for the "accelerated" scheme and  $\alpha = -1/2, \beta = -1$  for the "augmented-Lagrangian" one. Another scheme, the so-called "polarization" scheme where  $\langle \mathbf{P} \rangle$  is prescribed instead of  $\langle \mathbf{E} \rangle$ , can be described by an equation similar to (8) [19].

The alternative "variational" algorithm [14] relies on two distinct ideas. First, Eq. (3) is written as:

$$[(\sigma - \sigma^0)^{-1} \delta(\mathbf{x}) \delta_{ij} + G_{ij}^0] * P_j = \bar{E}_i. \quad (9)$$

Other FFT methods have been proposed, including an alternative "conjugate-gradient" scheme [21, 22] different from the "variational" one, and yet another one in which the convolution product is carried out in the direct space [23]. For conciseness, these and the "polarization" scheme alluded to above will not be considered further.

The dual formulation (4) allows one to derive dual algorithms for all FFT methods. For instance, substituting  $\mathbf{E}$ ,  $\mathbb{G}^0$  and  $\sigma^0$  by  $\mathbf{J}$ ,  $\mathbb{H}^0$  and  $\rho^0$  in Eq. (8) the dual "augmented-Lagrangian" scheme reads:

$$\mathbf{J}^{k+1} = \mathbf{J}^k + \frac{\rho^0 [\bar{\mathbf{J}} - \langle \mathbf{J}^k \rangle - \mathbb{H}^0 * (\frac{1}{\sigma} \mathbf{J}^k)] - \mathbb{G}^0 * \mathbf{J}^k}{1/\sigma + \rho^0}. \quad (10)$$

All of the above methods involve a reference conductivity  $\sigma^0$ , or a reference resistivity  $\rho^0$ . Whereas the final result is in principle independent of these quantities, their value have a dramatic influence on the convergence properties of the algorithms. Notably, optimal convergence of the "accelerated" scheme is obtained with the choice [17]

$$\sigma^0 = -\sqrt{\sigma_1 \sigma_2}, \quad (11)$$

where the use of a negative reference conductivity (devoid of physical meaning) is warranted by the arbitrary character of the reference medium. In this connection, we point out that in Ref. [20], which addresses the analogous elasticity problem, the reference stiffness moduli have their sign changed, which avoids dealing with negative values.

For the "direct" scheme, optimal convergence properties were studied in the context of elasticity [24]. Adapting the method used in the latter reference to the conductivity problem, it is straightforward to show that the corresponding optimal choice is

$$\sigma^0 = \frac{1}{2}(\sigma_1 + \sigma_2), \quad (12)$$

a result that we use extensively below.

### 4. CLASSICAL AND MODIFIED GREEN OPERATORS

In practice, the domain  $\Omega$  is discretized as a two-dimensional (2D) pixel image, or three-dimensional (3D) voxel image. The convolution product  $G_{ij}^0 * P_j$  in (3) is evaluated in the Fourier domain as

$$\int_{\Omega} d^d \mathbf{x}' G_{ij}^0(\mathbf{x} - \mathbf{x}') P_j(\mathbf{x}') \approx \frac{1}{L^d} \sum_{\mathbf{q}} G_{ij}^0(\mathbf{q}) P_j(\mathbf{q}) e^{i\mathbf{q} \cdot \mathbf{x}}, \quad (13)$$

where the Fourier mode components take on values  $q_i = (2\pi/L)(-L/2, \dots, L/2 - 1)$  ( $i = 1, \dots, d$ ), and  $L$  is measured in pixel/voxel size units. The vector  $P_j(\mathbf{q})$  is the Fourier transform

$$P_j(\mathbf{q}) = \sum_{\mathbf{x}} P_j(\mathbf{x}) e^{-i\mathbf{q}\cdot\mathbf{x}}, \quad (14)$$

where the sum is over all pixels/voxels  $\mathbf{x}$  in  $\Omega$ . Classically, the Fourier transform of the Green operator used in (13) is approximated by its continuum expression

$$G_{ij}^0(\mathbf{q}) = \int d^d\mathbf{x} G_{ij}^0(\mathbf{x}) e^{-i\mathbf{q}\cdot\mathbf{x}} = \frac{q_i q_j}{\sigma^0 |q|^2}, \quad (15)$$

where the integration is over the infinite domain and  $|q| = \sqrt{q_k q_k}$ . We call hereafter this version of the Green operator the “continuum” Green operator.

On the other hand, intrinsically discrete schemes can be considered. For instance, in the context of continuum mechanics, modified Green operators have been introduced, where partial derivatives are approximated by centered [25] or forward [26] differences. In the conductivity problem, the latter discretization amounts to solving a resistor network problem [27]:

$$\partial_i J_i(\mathbf{x}) \approx J_i(\mathbf{x}) - J_i(\mathbf{x} - \mathbf{e}_i), \quad \partial_i \Phi(\mathbf{x}) \approx \Phi(\mathbf{x} + \mathbf{e}_i) - \Phi(\mathbf{x}), \quad (16)$$

where  $J_i(\mathbf{x})$  represents the current along the bond pointing in the direction  $\mathbf{e}_i$  from point  $\mathbf{x}$  and  $\Phi(\mathbf{x})$  is the potential at node  $\mathbf{x}$ . The “discrete” Green operator  $\widetilde{\mathbb{G}}^0$  entering the corresponding Lippmann-Schwinger equation reads [26, 27]

$$\widetilde{G}_{ij}^0(\mathbf{k}) = \frac{k_i k_j^*}{\sigma^0 |k|^2}, \quad k_i = e^{iq_i} - 1 = 2i \sin(q_i/2) e^{iq_i/2}, \quad (17)$$

where  $|k| = \sqrt{k_i k_i^*}$  and  $*$  is the complex conjugate. Equation (17) reduces to (15) in the long-wavelength limit  $\mathbf{q} \rightarrow 0$ . In the dual setting, the discrete Green operator associated to the current is defined, mutatis mutandis, as in Eq. (5). The discretization employed in (16) locally enforces current conservation, which is not the case in FFT schemes based on Eq. (15).

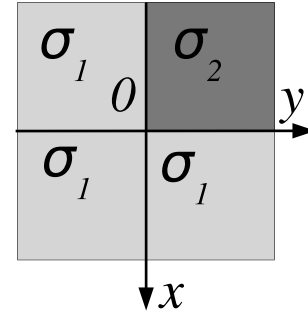
As long as they converge, all numerical schemes must deliver the same numerical results for a given choice of Green operator. Conversely, making a choice of Green operator will select one particular approximation to the solution of the problem considered. It is the purpose of this work to assess the advantages, from the numerical viewpoint, in the context of electrical conductivity, of using  $\widetilde{\mathbb{G}}^0$  in place of  $\mathbb{G}^0$ .

In this paper, the “direct” (DS), “accelerated” (AS), “augmented-Lagrangian” (AL), and “variational” (VAR) schemes are investigated. We also consider the dual versions of the “direct” and “augmented-Lagrangian” schemes, denoted by  $\text{DS}_D$  and  $\text{AL}_D$ , respectively. All of these make use of the continuum Green operator  $\mathbb{G}^0$ . Same algorithms, but with the *discrete* Green operator  $\widetilde{\mathbb{G}}^0$  instead of  $\mathbb{G}^0$  are also examined. They are referred to with a “tilde” notation as  $\widetilde{\text{DS}}$ ,  $\widetilde{\text{AS}}$ ,  $\widetilde{\text{AL}}$ ,  $\widetilde{\text{VAR}}$ ,  $\widetilde{\text{DS}}_D$ , and  $\widetilde{\text{AL}}_D$ .

In the “variational” approaches VAR and  $\widetilde{\text{VAR}}$  definite-positiveness of matrix  $\mathcal{M}$  (see Sec. 3) is not guaranteed in the conjugate-gradient procedure. This specific issue has not been considered further as numerical experiments we performed indicate that these schemes nevertheless converge.

## 5. A STIFF CASE: FIELDS IN THE FOUR-CELL MICROSTRUCTURE

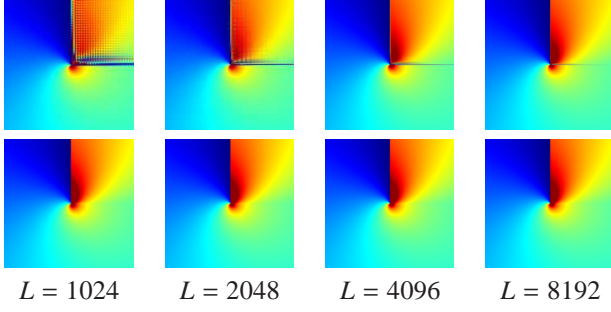
The “four-cell” microstructure is one of the few periodic structures for which an exact solution [28] is available. We consider the special case, represented in Fig. (1), where the elementary cell is made of a single square inclusion of surface fraction 25%. Due to the presence of corners, fields are singular in the infinite-contrast limit, which makes this case a good benchmark for numerical methods. In this Section, numerical results for the current computed with either the continuous Green operator  $\mathbb{G}^0$  or the discrete operator  $\widetilde{\mathbb{G}}^0$ , are compared with the exact solution. The inclusion is highly conducting, with a contrast ratio  $\sigma_2/\sigma_1 = 2 \times 10^3$ .



**Figure 1:** Elementary periodic domain  $\Omega = (-L/2, +L/2)^2$  with four-cell microstructure. The inclusion has conductivity  $\sigma_2$  and the matrix has conductivity  $\sigma_1$ .

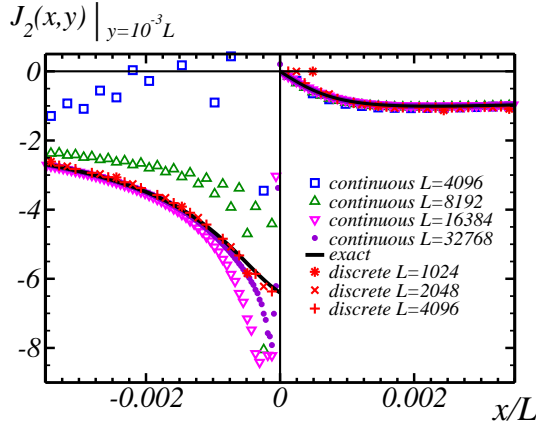
The behavior of the electrical current near the singular corner at point  $(x, y) = (0, 0)$  is illustrated in Fig. (2). Maps of the vertical component  $J_1(x, y)$  obtained with  $\mathbb{G}^0$  (top) and  $\widetilde{\mathbb{G}}^0$  (bottom) are displayed for increasing resolutions (left to right). Only the small region  $-5 \cdot 10^{-2}L \leq x, y \leq 5 \cdot 10^{-2}L$  around the corner is shown. Numerical artifacts in the highly-conducting phase are conspicuous when using the continuous Green operator  $\mathbb{G}^0$ . They consist of high-frequency oscillations all over the conducting region, particularly near the horizontal interface [29] where the represented field component should be continuous. Such oscillations are almost absent when using  $\widetilde{\mathbb{G}}^0$ .

Figure (3) displays plots of the horizontal component  $J_2(x, y)$  versus  $x$  at  $y = 10^{-3}L$ , i.e., close to the inclusion boundary. Negative values of  $x$  correspond to the interior of the inclusion. Numerical results computed with both Green operators are compared with the exact solution. To draw meaningful graphs, data points obtained with  $\mathbb{G}^0$  were post-processed prior to plotting by convolution over a window of



**Figure 2:** Four-cell microstructure of Fig. 1. Maps of the vertical current component  $J_1(x, y)$  in the region  $-0.05L \leq x, y \leq 0.05L$ , for increasing resolution  $L$  (as indicated). Top: with continuous Green operator  $\mathbb{G}^0$ . Bottom: with discrete operator  $\widetilde{\mathbb{G}}^0$ .

$2 \times 2$  adjacent pixels. This crude filtering device greatly reduces oscillations. Results obtained with  $\widetilde{\mathbb{G}}^0$  have not been modified. Given sufficient resolution all methods converge to the exact solution. However, while all methods lead to almost identical solutions in the matrix, results strongly differ in the highly-conducting region. The figure, which represents calculations carried out for various resolutions, shows that employing  $\widetilde{\mathbb{G}}^0$  makes convergence notably easier. Indeed, data points obtained with  $\widetilde{\mathbb{G}}^0$  at moderate resolution  $L = 1024$  are much closer to the exact solution than those obtained from  $\mathbb{G}^0$  at the highest resolution  $L = 32768$ .



**Figure 3:** Four-cell microstructure of Fig. 1. Values of the horizontal current component  $J_2(x, y = 10^{-3}L)$  vs.  $x$ , for various resolutions  $L$  (as indicated). Solid black: exact solution. Markers \*,  $\times$  and + (red): FFT results with discrete Green operator  $\widetilde{\mathbb{G}}^0$ . Other markers and colors: FFT results with continuous Green operator  $\mathbb{G}^0$ .

In a previous study involving porous media [26] the continuous Green operator was already observed to induce awkward aliasing effects at high contrast. They usually take place near interfaces involving a region where the field considered is not uniquely defined in the infinite-contrast limit

(e.g., the strain in a pore, or the electric current in an infinitely-conducting inclusion).

## 6. CONVERGENCE RATE

This Section further examines for a few selected microstructures the convergence properties of FFT schemes. Algorithmic convergence being harder in the case of strongly-contrasted composites, the quantity of interest here is the number of iterations as a function of the contrast ratio  $\sigma_2/\sigma_1$ .

### 6.1. Convergence criteria

Convergence criteria can be written either in the direct or Fourier representations. The most compelling ones are those that include high Fourier-frequency behavior [20]. In relation to FFT algorithms, the following criteria are considered:

$$\eta_1 = \frac{1}{\|\mathbf{J}\|} \max_{\mathbf{x}} |\text{FT}^{-1} \{k_i(\mathbf{q})J_i(\mathbf{q}); \mathbf{x}\}| \leq \epsilon, \quad (18a)$$

$$\eta_2 = \frac{1}{\|\mathbf{E}\|} \max_{i \neq j, \mathbf{x}} |\text{FT}^{-1} \{k_i(\mathbf{q})E_j(\mathbf{q}) - k_j(\mathbf{q})E_i(\mathbf{q}); \mathbf{x}\}| \leq \epsilon, \quad (18b)$$

where  $\epsilon \ll 1$  is the required precision and  $\text{FT}^{-1}$  is the backward Fourier transform. Criterion (18a) put emphasis on current conservation while (18b) imposes compatibility; apart from a difference in the norm used, they are akin to those used in [20]. The above writings refer to the discrete Green operator  $\widetilde{\mathbb{G}}^0$ . The quantity  $\mathbf{k}(\mathbf{q})$  should be replaced by  $\mathbf{q}$  when the continuous Green operator  $\mathbb{G}^0$  is used instead.

Among the computational schemes introduced in Sec. 4, the “direct” (DS and  $\widetilde{\text{DS}}$ ) and “augmented-Lagrangian” (AL and  $\widetilde{\text{AL}}$ ) schemes enforce compatibility at each iteration, which trivially guarantees that  $\eta_2 = 0$ . Instead, electric current conservation in the form of the equality  $\eta_1 = 0$  is enforced by the dual schemes  $\text{DS}_D$ ,  $\widetilde{\text{DS}}_D$ ,  $\text{AL}_D$  and  $\widetilde{\text{AL}}_D$ . On the other hand, the remaining schemes in general lead to nonzero values of  $\eta_1$  and  $\eta_2$ . This suggests using as a convergence criterion the inequality  $\eta \leq \epsilon$  where  $\eta = \eta_1$  for the primary (non-dual) schemes DS,  $\widetilde{\text{DS}}$ , AL,  $\widetilde{\text{AL}}$ , AS,  $\widetilde{\text{AS}}$ , VAR, and where  $\eta = \eta_2$  for the dual ones  $\text{DS}_D$ ,  $\widetilde{\text{DS}}_D$ ,  $\text{AL}_D$ ,  $\widetilde{\text{AL}}_D$ .

### 6.2. Test microstructures

Convergence rates are monitored for three microstructures, periodic in all directions, whose unit cells  $\Omega$  are represented in Fig. (4). The leftmost 2D cell, of size  $L = 1024$  pixels, contains a single circular disk-shaped inclusion of surface fraction 25%. This system is simply referred to as the “2D-periodic” medium hereafter. The middle cell is a random 2D Boolean model of size  $L = 1024$  built from disks of diameter 80 pixels, of overall surface fraction 30%. The rightmost cell is a random 3D Boolean model of size  $L = 256$ , made

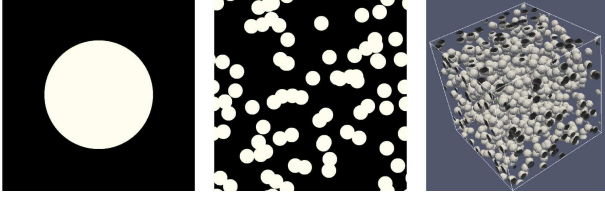


**Figure 4:** Elementary cell  $\Omega$  of the “2D-periodic” microstructure (left), and the 2D (center) and 3D (right) random periodic Boolean models. Surface and volume fractions of the inclusions are, respectively, 25, 30 and 20%.

of spherical inclusions of diameter 20 voxels, with overall volume fraction 20%.

### 6.3. 2D periodic medium

Figure (5) illustrates for some of the algorithms introduced in Sec. 4 applied to the “2D-periodic” medium how the indicator  $\eta$  tends to zero as the number of iterations increases. The contrast ratio is fixed at  $\sigma_2/\sigma_1 = 2 \times 10^3$ . For exploratory purposes, quadruple precision was used in these calculations to allow for tiny values of  $\eta$ . Prior to drawing the plots, the quantities  $\sigma^0$  and  $\rho^0$  were optimized manually to minimize the number of iterations needed to reach the arbitrary threshold  $\eta < \epsilon = 10^{-12}$ . For all methods  $\eta$  decreases exponentially with the number of iterations down to some constant value determined by machine precision. Roughly, algorithms separate in two classes. The first one comprises the “continuous” schemes, namely, DS, AL and AS, which are the slowest-converging ones. However, in this class and for the microstructure considered, Eyre and Milton’s AS method is clearly superior. The simple “direct” scheme DS is by far the worst, and the “augmented-Lagrangian” AL scheme is intermediate. The other class encompasses the “discrete” schemes (primary and dual). They all make  $\eta$  saturate in less than 300 iterations, which is another hint at the good behavior of the discrete Green operator. In that class, Eyre and Milton’s method ( $\widetilde{AS}$ ) again proves the fastest-converging one.

The optimal reference conductivity  $\sigma^0$  and resistivity  $\rho^0$  used in Fig. (5) are summarized in the second column of Tab. (1). The integer number in brackets is the number of iterations needed to reach the threshold  $\eta < \epsilon = 10^{-8}$ , which in practice is a good trade-off between speed and accuracy. With the “direct” scheme, Eq. (12) optimizes scheme DS with the continuous Green operator. It gives  $\sigma^0 = 1000.5$  and —this is an empirical finding— optimizes also scheme  $\widetilde{DS}$  with the discrete Green operator. Introducing the phase resistivities as  $\rho_{1,2} = 1/\sigma_{1,2}$  an analogous formula (easy to demonstrate in the continuum) holds for the optimal resistivity in the continuous dual “direct” scheme  $DS_D$ , namely,

$$\rho^0 = \frac{1}{2}(\rho_1 + \rho_2), \quad (19)$$

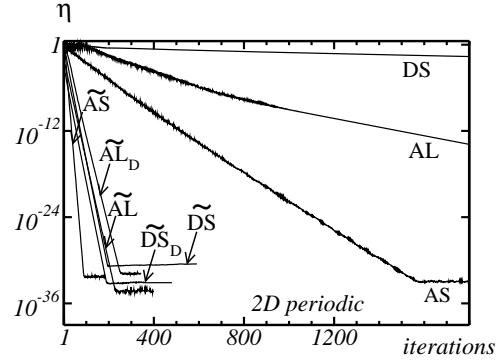


**Figure 5:** “2D-periodic” medium. Convergence indicator  $\eta$  vs. number of iterations in logarithmic-linear scale, for various FFT schemes: using the continuum Green operator (DS, AS, and AL), and the discrete Green operator ( $\widetilde{DS}$ ,  $\widetilde{DS}_D$ ,  $\widetilde{AS}$ ,  $\widetilde{AL}$  and  $\widetilde{AL}_D$ ).

which provides here the value  $\rho^0 \approx 0.5$ . Again empirically, we find that this value optimizes as well the discrete dual “direct” scheme  $\widetilde{DS}_D$ . As expected, the optimum  $\sigma^0 \approx -44.7$  reported for scheme AS matches Eyre and Milton’s result, Eq. (11). However, although negative, the optimum  $\sigma^0$  found for the discrete scheme  $\widetilde{AS}$  is *not* consistent with this formula. Finally, the values reported for the primary augmented-Lagrangian schemes AL and  $\widetilde{AL}$  and their dual versions do not match any of the previous analytical estimates.

### 6.4. 2D and 3D Boolean media: reference conductivity or resistivity

A more thorough study was carried out for the Boolean models, in which the optimal reference conductivity  $\sigma^0$  or resistivity  $\rho^0$  was measured as a function of the contrast.

In order to avoid unnecessary long computations, the reference was first manually optimized on a low-resolution grid of size  $L = 64$  (in 2D) or  $L = 32$  (in 3D). The optimized reference was then tested on a full-resolution grid of size  $L = 1024$  (2D) or  $L = 256$  (3D). In all but a handful of cases, the numbers of iterations to convergence found with the low- and high-resolution grids were nearly the same. The number of iterations found on the full-resolution grid was kept if the difference was less than 10%; otherwise, the reference was optimized again, this time on the full-resolution grid, to provide a definitive number of iterations. Manual optimization of the reference parameters was carried out following a rough dichotomy procedure, disregarding for simplicity the possibility of concurrent local optima. The convergence criterion was set to  $\eta \leq \epsilon = 10^{-8}$  in these calculations.

Our findings are summarized in the third and fourth columns of Tab. (1), where the formulas given essentially represent the high-contrast behaviors, i.e., the regimes  $\sigma_2/\sigma_1 \ll 1$  or  $\sigma_2/\sigma_1 \gg 1$ . Indeed, in some cases the low-contrast behavior may differ from that given (see below).

At the exception of scheme  $\widetilde{AS}$  in the 3D Boolean

$\sigma^0$			
	“2D-periodic”	2D Boolean	3D Boolean
DS	1000.5 (15621)	$(\sigma_1 + \sigma_2)/2$	$(\sigma_1 + \sigma_2)/2$
AL	76 (1556)	$3 \cdot 10^{-3} \sigma_1 + 1.8 \sqrt{\sigma_1 \sigma_2}$	$1.7 \sqrt{\sigma_1 \sigma_2}$
AS	-44.7 (663)	$-\sqrt{\sigma_1 \sigma_2}$	$-\sqrt{\sigma_1 \sigma_2}$
VAR	N/A	$0.50(\sigma_1 + \sigma_2)$	N/A
$\widetilde{\text{DS}}$	1000.5 (46)	$0.50(\sigma_1 + \sigma_2)$	$0.53\sigma_1 + 0.50\sigma_2$
$\widetilde{\text{AL}}$	1855 (95)	$0.30(\sigma_1 + \sigma_2)$	$0.56\sigma_1 + 0.26\sigma_2$
$\widetilde{\text{AS}}$	-1390 (46)	$-0.30(\sigma_1 + \sigma_2)$	$-(1/3.6)\sigma_1$ ( $\sigma_2/\sigma_1 \ll 1$ ) $-3.6\sigma_1$ ( $\sigma_2/\sigma_1 \gg 1$ )
$\widetilde{\text{VAR}}$	N/A	$0.50(\sigma_1 + \sigma_2)$	N/A
$\rho^0$			
DS <sub>D</sub>	0.5 (14616)	$(\rho_1 + \rho_2)/2$	$(\rho_1 + \rho_2)/2$
AL <sub>D</sub>	0.033 (1336)	$3 \cdot 10^{-3} \rho_1 + 1.8 \sqrt{\rho_1 \rho_2}$	$1.7 \sqrt{\rho_1 \rho_2}$
$\widetilde{\text{DS}}_D$	0.5 (46)	$0.50(\rho_1 + \rho_2)$	$0.48\rho_1 + 0.52\rho_2$
$\widetilde{\text{AL}}_D$	1.09 (93)	$0.30(\rho_1 + \rho_2)$	$0.40\rho_1 + 0.55\rho_2$

**Table 1:** Optimal reference conductivities  $\sigma^0$  and resistivities  $\rho^0$  determined for the indicated FFT schemes. Values given for the “2D-periodic” microstructure correspond to the contrast ratio  $\sigma_2/\sigma_1 = 2 \times 10^3$ , with the number of iterations indicated in brackets. For Boolean models, the formulas given are consistent with the behavior observed at high contrast, although the low-contrast behavior may slightly differ. Those for schemes DS, AS and DS<sub>D</sub> are exact ones. Missing entries (N/A) indicate that the corresponding schemes have not been investigated.

medium, for which  $\sigma^0/\sigma_1$  tends to a constant at high contrast—notice the symmetry between both high-contrast regimes, the behaviors we observed are of the following types

$$\sigma^0/\sigma_1 = \alpha_1 + \alpha_2 r, \quad (20a)$$

$$\text{or } \sigma^0/\sigma_1 = \beta_1 + \beta_2 r^{1/2}, \quad (20b)$$

where  $r = \sigma_2/\sigma_1$ , and  $\alpha_{1,2}$  and  $\beta_{1,2}$  are numerical constants of various signs (see Table). These forms generalize Eqs. (11) and (12). They apply to the “primary” schemes, and similar ones hold for the “dual” schemes with  $\sigma$  substituted by  $\rho$ . When nonzero, the coefficient  $\beta_1$ , of order  $10^{-3}$ , is of unclear origin. The coefficients reported in the Table were determined by non-linear least-square fitting on our data. Additional fitting attempts with functional forms other than (but related to) those retained indicate that the first digit of the coefficients is significant, while the error on the second one is hard to evaluate. Different coefficients  $\alpha_1$  and  $\alpha_2$  are provided when our results do not support an equality  $\alpha_1 = \alpha_2$ . However, our results strongly suggest that  $\alpha_1 = \alpha_2$  for the 2D Boolean system whenever Eq. (20a) applies, while this symmetry does not carry over to the 3D case, except for the “direct” scheme where  $\alpha_1 = \alpha_2 = 1/2$  (exact) in two and three dimensions.

Although the optimum may in some cases be of the same form with the continuous and discrete Green operators, there are other cases such as with the AS and  $\widetilde{\text{AS}}$  schemes, for which the optimal forms look strongly dissimilar. Moreover, comparing columns two and three of the Table for the contrast  $\sigma_2/\sigma_1 = 2 \times 10^3$  indicates that the optima found somewhat depend on the microstructure.

The behaviors gathered in the Table are supported by Figs. 6 and 7, which presents plots of our 2D and 3D data, and the corresponding fitting curves. The “primary” and “dual” schemes are addressed in separate plots. The signs indicated in the Table cannot be read from the figures where absolute values are displayed in logarithmic scale. In the 2D Boolean model the data for the primary schemes and for their dual are numerically quite close in this mode of representation, so that the left and right plots superimpose almost exactly. Interestingly, the plots reveal the unique non-trivial behavior of the discrete schemes  $\widetilde{\text{AL}}$  and  $\widetilde{\text{AL}}_D$  in the low-contrast region  $0.1 \leq \sigma_2/\sigma_1 \leq 10$ , where they behave as  $\sqrt{\sigma_2/\sigma_1}$  even though the linear behavior reported in Tab. (1) takes place at higher contrasts. On the other hand, the continuous schemes AL and AL<sub>D</sub> essentially behave as a square root for all contrasts (up to a small corrective term in 2D cases). As already noticed in the discussion of the Table, the discrete 3D “accelerated” scheme  $\widetilde{\text{AS}}$  with its intriguing asymptotic behavior (constant on both sides of the contrast range) stands as an outlier. For it no fit has been attempted. We emphasize that in all cases examined with the “accelerated” schemes, the optimal square-root estimate (11)—exact in scheme AS—yields poor convergence when applied to scheme  $\widetilde{\text{AS}}$ .

We also investigated the sensitivity to the choice of  $\sigma^0$  in the “direct” discrete schemes. In the 2D Boolean model and for the discrete scheme  $\widetilde{\text{DS}}$  the choice  $\sigma^0 = 0.50(\sigma_1 + \sigma_2)$  proves optimal, which matches the exact result relative to scheme DS. However, with  $\widetilde{\text{DS}}$  nearly optimal 2D results are also obtained with choices  $\sigma^0 < (\sigma_1 + \sigma_2)/2$ . By contrast, in 3D the number of iterations may be extremely sensitive

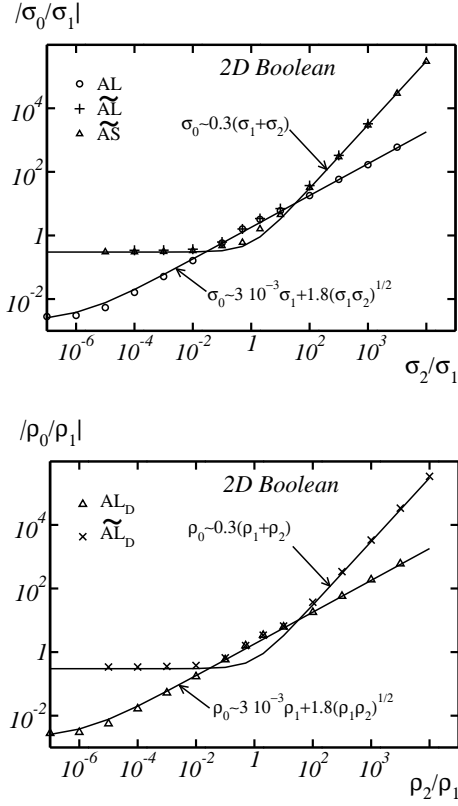


**Figure 6:** 2D Boolean models. Absolute value of the normalized optimal conductivity  $|\sigma^0/\sigma_1|$  vs.  $\sigma_2/\sigma_1$  (top), and optimal resistivity  $|\rho_0/\rho_1|$  vs.  $\rho_2/\rho_1$  (bottom), for the schemes indicated. Symbols: FFT results. Solid: numerical fits (see Tab. 1).

to the choice of  $\sigma^0$ . Figure (8) illustrates this. It represents the number of iterations vs.  $\sigma^0$  for the scheme  $\widetilde{DS}$  in the 3D Boolean model, with contrast  $\sigma_2/\sigma_1 = 10^{-5}$ . No convergence is observed for  $\sigma^0 < 0.5(\sigma_1 + \sigma_2)$ , and the optimal choice is about  $\sigma^0 \approx 0.53\sigma_1$ .

### 6.5. 2D and 3D Boolean media: convergence properties

This Section examines convergence performance for the 2D and 3D Boolean models, expressed by the number of iterations  $N$  as a function of the contrast ratio  $r = \sigma_2/\sigma_1$ . Figure (9) illustrates the performance of the various FFT schemes considered, in calculations optimized by using the reference conductivity or resistivity discussed in the previous section. Schemes using  $\mathbb{G}^0$  are represented by filled symbols and the + marker, whereas discrete schemes using  $\widetilde{\mathbb{G}}^0$  are represented by empty symbols and the × marker.

We recover known results of linear scaling  $N \sim r$  for the “direct” schemes DS and  $DS_D$ , and of square-root scaling  $N \sim r^{1/2}$  for the “accelerated” scheme AS [17]. Similar convergence rates are observed for the “augmented-Lagrangian” schemes AL and  $AL_D$ , and the “variational” one, VAR. As a rule, given the FFT method the “primary” scheme always converges better than the “dual” one when  $r < 1$ , while the

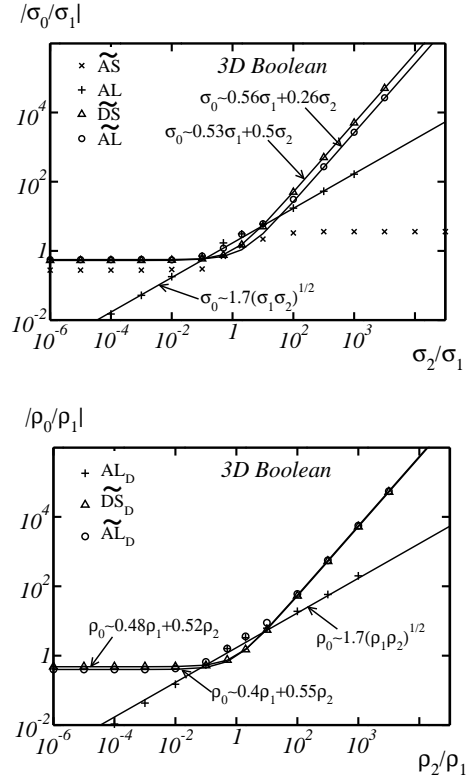


**Figure 7:** 3D Boolean models. Absolute value of the normalized optimal conductivity  $|\sigma^0/\sigma_1|$  vs.  $\sigma_2/\sigma_1$  (top), and optimal resistivity  $|\rho_0/\rho_1|$  vs.  $\rho_2/\rho_1$  (bottom), for the schemes indicated. Symbols: FFT results. Solid: numerical fits (see Tab. 1).

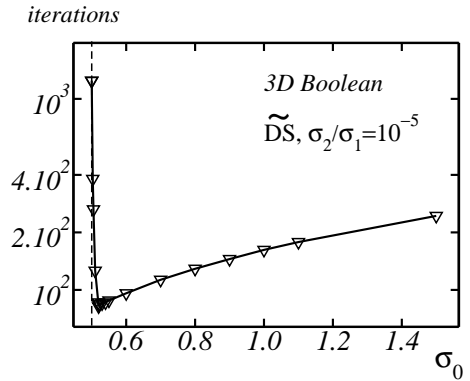


**Figure 8:** 3D Boolean model. Number of iterations vs. reference conductivity  $\sigma^0$  for the direct scheme with discrete Green operator ( $\widetilde{DS}$ ). The contrast ratio is  $\sigma_2/\sigma_1 = 10^{-5}$ . The convergence criterion is  $\eta \leq \epsilon = 10^{-8}$ . The value  $\sigma^0 = (\sigma_1 + \sigma_2)/2$  is represented by the vertical dotted line. The solid line between data points is a guide to the eye.

opposite holds when  $r > 1$ . For instance, at very strong contrast ratio  $r > 10^7$ , the convergence of the dual “augmented-Lagrangian” scheme  $AL_D$  is much faster than that of the primary scheme AL.



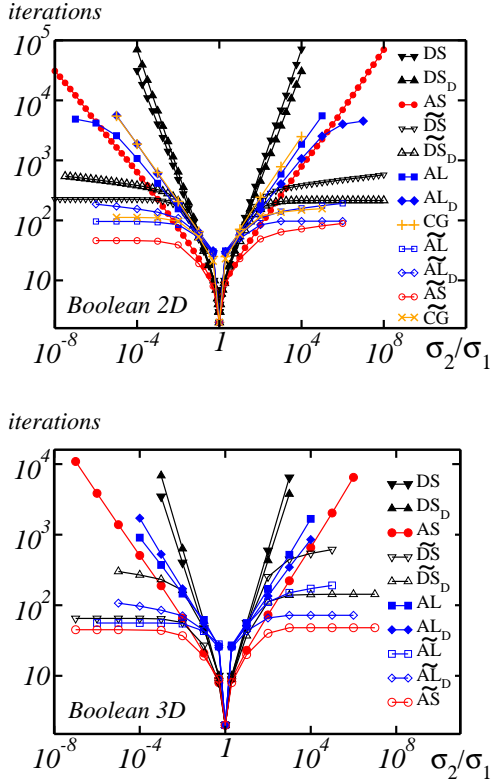


**Figure 9:** 2D and 3D Boolean models. Number of iterations vs. contrast for various FFT algorithms. The convergence criterion is  $\eta \leq \epsilon = 10^{-8}$ . Solid lines between data points are guides to the eye.

As to discrete schemes, they are much more efficient than their continuum counterparts. For discrete schemes  $N(r)$  is either a bounded or slowly-increasing function of  $r$ , which shows that using the discrete Green operator  $\widetilde{\mathbb{G}}^0$  definitely provides a dramatic improvement of convergence. By optimizing the choice between the “primary” or “dual” versions of the discrete algorithm at hand depending on whether  $r < 1$  or  $r > 1$ , one can even achieve *convergence in a finite number of iterations* in the infinite-contrast limit.

Overall, the figure shows that among all schemes the discrete version  $\widetilde{\text{AS}}$  of the “accelerated” scheme is the better-converging one in 2D and 3D.

## 7. OPTIMIZING THE “DIRECT” SCHEME WITH DISCRETE GREEN OPERATOR

In applications dealing with large microstructures (typically, multiscale materials) fast and memory-efficient implementations of FFT methods are required. One common way of minimizing both CPU speed and memory storage is to recompute the Green operator at each iteration. As long as the Green operator is easy to compute, this strategy is usually faster than storing a very large tensor field. This is used in the CraFT [30] and morph-Hom [31] softwares. As an ex-

ample, a low-cost implementation of the “direct” scheme DS is as follows:

Initialization: set  $A_i(\mathbf{x}) \equiv 0$ .

- i. Set  $A_i(\mathbf{x}) := [\sigma(\mathbf{x}) - \sigma^0]A_i(\mathbf{x})$ ;
- ii. Set  $A_i(\mathbf{q}) := \text{FFT}\{A_i(\mathbf{x}); \mathbf{q}\}$ ;
- iii. Set  $A_i(\mathbf{q}) := G_{ij}^0(\mathbf{q})A_j(\mathbf{q})$  for  $\mathbf{q} \neq 0$  and  $A_i(\mathbf{q} = 0) := \overline{E}_i$ ; compute the convergence criterion  $\eta$ ;
- iv. Set  $A_i(\mathbf{x}) := \text{FFT}^{-1}\{A_i(\mathbf{q}); \mathbf{x}\}$ ;
- v. If  $\eta \leq \epsilon$ , set  $E_i = A_i$  and STOP; otherwise GOTO (i).

In this algorithm FFTs are computed *in-place*. In total, memory space is allocated for one vector field  $\mathbf{A}$ , plus the microstructure. Vector  $\mathbf{A}$  successively stores the polarization field in the real space [step (i)] and in the Fourier domain [step (ii)] and the electrical field  $\mathbf{E}$  in the Fourier domain [step (iii)] and real space [step (iv)].

On the other hand, use of the discrete Green operator  $\widetilde{\mathbb{G}}^0$  allows for a more efficient implementation of the “direct” scheme. Consider the rewriting of Eq. (7) as:

$$\phi^{k+1} = \frac{1}{\sigma^0 \Delta} \mathbf{div} [(\sigma - \sigma^0)(\overline{\mathbf{E}} - \mathbf{grad} \phi^k)] \quad (21)$$

where  $\phi^k$  is the periodic part of the potential associated to  $\mathbf{E}^k$ , so that  $\mathbf{E}^k - \overline{\mathbf{E}} = -\mathbf{grad} \phi^k$ , and where  $1/\Delta$  is, symbolically, the inverse Laplacian. Equation (21) defines  $\phi^{k+1}$  as a unique periodic function up to an irrelevant constant. When  $k \rightarrow \infty$ ,  $\phi^k$  converges to the potential up to a linear correction  $\phi^\infty(\mathbf{x}) = \Phi(\mathbf{x}) - \overline{E}_i x_i$ . The electrical and current fields follow from  $\Phi$ . In the discrete setting, equivalent to a resistor network, knowledge of a field on adjacent nodes or bonds is sufficient to compute its local divergence or gradient. Thus, the action of applying operators  $\mathbf{div}$  and  $\mathbf{grad}$  that enter Eq. (21) can be computed in the real space. This suggests the following alternative implementation of the discrete direct scheme (DS).

Initialization: set  $A(\mathbf{x}) \equiv 0$ .

- i. At each point  $\mathbf{x}$ , set  $A(\mathbf{x}) := \mathbf{div} \mathbf{P}(\mathbf{x})$  where  $P_i(\mathbf{x}) = [\sigma(\mathbf{x}) - \sigma^0][\overline{E}_i - \mathbf{grad} A(\mathbf{x})]$ ; compute  $\eta_1$  as defined in (18);
- ii. Set  $A(\mathbf{q}) := \text{FFT}\{A(\mathbf{x}); \mathbf{q}\}$ ;
- iii. Set  $A(\mathbf{q}) := -\frac{A(\mathbf{q})}{\sigma^0 |k(\mathbf{q})|^2}$  for  $\mathbf{q} \neq 0$  and  $A(\mathbf{q} = 0) := 0$  otherwise;
- iv. Set  $A(\mathbf{x}) := \text{FFT}^{-1}\{A(\mathbf{q}); \mathbf{x}\}$ ;
- v. If  $\eta_1 < \epsilon$  set  $\mathbf{E} = \overline{\mathbf{E}} - \mathbf{grad} A$ ,  $\mathbf{J} = \sigma \mathbf{E}$  and STOP; otherwise GOTO (i).

This algorithm exactly implements the  $\widetilde{\text{DS}}$  scheme. However only a scalar field, rather than a vector field, is now allocated in memory. Step (i) is carried out in the real space by means

of finite differences whereas the Laplacian inversion in step (iii) is computed in the Fourier domain. The field  $A$  successively stores the divergence of the polarization field  $\mathbf{div} \mathbf{P}$  in the real space [step (i)] and Fourier domain [step (ii)] and, later on, the periodic part of the potential  $\phi$  in the Fourier domain [step (iii)] and in the real space [step (iv)]. Multi-threading parallelization in step (i) necessitates some care as this step is non-local. Nevertheless, this new implementation reduces the number of FFTs per iteration from 4 (in 2D) or 6 (in 3D) down to 2. Furthermore, the amount of storage is also reduced by a factor  $d$  ( $L^d$  floats instead of  $dL^d$ ), if we neglect the storage required for the microstructure.

The total CPU time spent using “direct”, “augmented-Lagrangian” and “accelerated” schemes is plotted in Fig. (10) as a function of contrast, the scheme  $\widetilde{DS}$  being implemented as outlined above. These tests were carried out with convergence criterion  $\eta < 10^{-8}$ , on the previously-considered 3D Boolean microstructure discretized on a grid of size  $L = 256$  (16.8 million points). Computations were performed in double precision, on a 12-core Intel Xeon machine, each core running at 2.90 GHz with 5800 bogomips and 15360 Kb of L2 cache. Best performance is achieved for the  $\widetilde{DS}$  scheme when  $\sigma_2/\sigma_1 < 1$ , and with the “accelerated” scheme  $\widetilde{AS}$  when  $\sigma_2/\sigma_1 > 1$ . Using these optimal schemes at infinite contrast, convergence is completed in 29 seconds for insulating inclusions, and in 53 seconds for infinitely-conducting inclusions. This strategy has been implemented in the multithreaded Fortran code *morph-hom* developed at Mines ParisTech [31].

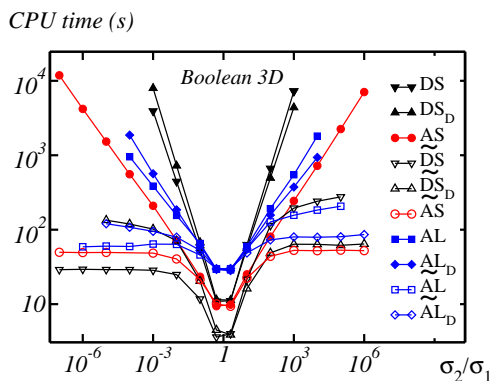


**Figure 10:** CPU time vs. contrast ratio  $\sigma_2/\sigma_1$  for various FFT algorithms, on the 3D Boolean microstructure. The convergence criterion is  $\eta \leq \epsilon$  with  $\epsilon = 10^{-8}$ .

## 8. CONCLUSION

Use of a modified Green operator in FFT-based schemes has been advocated, in the context of the electrical response of heterogeneous conducting media. The modification consists in making the operator consistent with the underlying voxel grid, which requires only a very simple adaptation of

previously-existing algorithms, but leads to two major improvements.

First, employing the modified operator leads to much more accurate local fields, particularly in highly-conducting or insulating inclusions, and in the vicinity of interfaces. Second, the convergence rate is found to be much faster compared with previous methods, in particular for highly-contrasted media. Quite remarkably the “direct” scheme—usually considered to be the worst-converging one—improves tremendously, as far as CPU time is concerned, by formulating the problem in terms of iterations on the electrostatic potential rather than on the electric field. However, use of the modified Green operator requires carefully adjusting the reference conductivity  $\sigma^0$ , since the latter has a strong influence on the convergence properties. Approximate expressions for  $\sigma^0$  have been derived numerically, and studied, for the Boolean models of microstructure considered in this work.

That using “discrete” versions of Green operators leads to promising methods has already been noticed [14, 26]. Demonstrating that dramatic speed-up improvements follow, the present work strongly supports this view. Based on previous experience [26], it is expected that the above conclusions carry over to continuum mechanics.

## ACKNOWLEDGEMENTS

The authors are grateful to H. Moulinec for kindly providing some field maps for comparison purposes, which has been a very helpful assistance in this study. The research leading to the results presented has received funding from the European Union’s Seventh Framework Programme (FP7 / 2007-2013) for the Fuel Cells and Hydrogen Joint Technology Initiative under grant agreement 303429.

## REFERENCES

- [1] H. Moulinec, P. Suquet, A fast numerical method for computing the linear and non linear mechanical properties of the composites, *Comptes rendus de l’Academie des sciences, Série II* 318 (11) (1994) 1417–1423.
- [2] F. Willot, Y. Pellegrini, M. Idiart, P. Castañeda, Effective-medium theory for infinite-contrast two-dimensionally periodic linear composites with strongly anisotropic matrix behavior: dilute limit and crossover behavior, *Physical review B* 78 (10) (2008) 104111.
- [3] R. Lebensohn, N-site modeling of a 3D viscoplastic polycrystal using fast Fourier transform, *Acta Materialia* 49 (14) (2001) 2723–2737.
- [4] J. Li, S. Meng, X. Tian, F. Song, C. Jiang, A non-local fracture model for composite laminates and numerical simulations by using the fft method, *Composites Part B: Engineering* 43 (3) (2011) 961–971.
- [5] F. Willot, L. Gillibert, D. Jeulin, Microstructure-induced hotspots in the thermal and elastic responses

- of granular media, *International Journal of Solids and Structures* 50 (10) (2013) 1699–1709.
- [6] F. Willot, D. Jeulin, Elastic and electrical behavior of some random multiscale highly-contrasted composites, *International Journal for Multiscale Computational Engineering: special issue on Multiscale modeling and uncertainty quantification of heterogeneous materials* 9 (3) (2011) 305–326.
- [7] D. Azzimonti, F. Willot, D. Jeulin, Optical properties of deposit models for paints: full-fields FFT computations and representative volume element, *Journal of Modern Optics* 60 (7) (2013) 519–528.
- [8] A. Jean, F. Willot, S. Cantournet, S. Forest, D. Jeulin, Large-scale computations of effective elastic properties of rubber with carbon black fillers, *International Journal for Multiscale Computational Engineering* 9 (3) (2011) 271–303.
- [9] A. Belkhabbaz, R. Brenner, N. Rupin, B. Bacroix, J. Fonseca, Prediction of the overall behavior of a 3d microstructure of austenitic steel by using fft numerical scheme, *Procedia Engineering* 10 (2011) 1883–1888.
- [10] A. Prakash, R. Lebensohn, Simulation of micromechanical behavior of polycrystals: finite element versus fast Fourier transforms, *Modelling Simul. Mater. Sci. Eng.* 17 (6) (2009) 064010.
- [11] A. Rollett, R. Lebensohn, M. Groeber, Y. Choi, L. J., R. G.S., Stress hot spots in viscoplastic deformation of polycrystals, *Modelling and Simulation in Material Science and Engineering* 18 (7) (2010) 074005.
- [12] R. Lebensohn, O. Castelnau, R. Brenner, P. Gilormini, Study of the antiplane deformation of linear 2-d polycrystals with different microstructures, *International journal of solids and structures* 42 (20) (2005) 5441–5459.
- [13] C. Dunant, B. Bary, A. Giorla, C. Pniguel, J. Sanahuja, C. Toulemonde, A. Tran, F. Willot, J. Yvonnet, A critical comparison of several numerical methods for computing effective properties of highly heterogeneous materials, *Advances in Engineering Software* 58 (2013) 1–12.
- [14] S. Brisard, L. Dormieux, FFT-based methods for the mechanics of composites: A general variational framework, *Computational Materials Science* 49 (3) (2010) 663–671.
- [15] T. Kanit, S. Forest, I. Galliet, V. Mounoury, D. Jeulin, Determination of the size of the representative volume element for random composites: statistical and numerical approach, *International Journal of Solids and Structures* 40 (13–14) (2003) 3647–3679.
- [16] G. W. Milton, *The Theory of Composites*, Cambridge Univ. Press, Cambridge, 2002.
- [17] D. Eyre, G. Milton, A fast numerical scheme for computing the response of composites using grid refinement, *The European Physical Journal Applied Physics* 6 (1) (1999) 41–47.
- [18] J.-C. Michel, H. Moulinec, P. Suquet, A computational scheme for linear and non-linear composites with arbitrary phase contrast, *International Journal for Numerical Methods in Engineering* 52 (1-2) (2001) 139–160.
- [19] V. Monchiet, G. Bonnet, A polarization-based FFT iterative scheme for computing the effective properties of elastic composites with arbitrary contrast, *International Journal for Numerical Methods in Engineering* 89 (11) (2012) 1410–1436.
- [20] H. Moulinec, F. Silva, Comparison of three accelerated FFT-based schemes for computing the mechanical response of composite materials.
- [21] J. Zeman, J. Vodrejc, J. Novak, I. Marek, Accelerating a FFT-based solver for numerical homogenization of a periodic media by conjugate gradients, *Journal of Computational Physics* 229 (21) (2010) 8065–8071.
- [22] B. Vondřejc, J. Zeman, I. Marek, Analysis of a fast Fourier transform based method for modeling of heterogeneous materials, *Large-Scale Scientific Computing* 7116 (2012) 515–522.
- [23] J. Yvonnet, A fast method for solving microstructural problems defined by digital images: a space Lippmann–Schwinger scheme, *International Journal for Numerical Methods in Engineering* 92 (2) (2012) 178–205.
- [24] H. Moulinec, P. Suquet, A numerical method for computing the overall response of nonlinear composites with complex microstructure, *Computer Methods in Applied Mechanics and Engineering* 157 (1) (1998) 69–94.
- [25] W. H. Müller, Mathematical vs. experimental stress analysis of inhomogeneities in solids, *Journal de Physique* 6 (C1) (1996) 139–148.
- [26] F. Willot, Y.-P. Pellegrini, Fast Fourier transform computations and build-up of plastic deformation in 2D, elastic-perfectly plastic, pixelwise-disordered porous media, in: D. Jeulin, S. Forest (eds), “Continuum Models and Discrete Systems CMDS 11”, École des Mines, Paris, 2008, pp. 443–449.
- [27] J.-M. Luck, Conductivity of random resistor networks: an investigation of the accuracy of the effective-medium approximation, *Physical Review B* 43 (5) (1991) 3933–3944.
- [28] R. Craster, Y. Obnosov, Four phase checkerboard composites, *SIAM Journal on Applied Mathematics* 61 (6) (2001) 1839–1856.
- [29] This oscillatory behavior was confirmed in elasticity by H. Moulinec using independent software (private communication, 2013). it is similar to that reported in [26].
- [30] CraFT software, <http://craft.lma.cnrs-mrs.fr/>, accessed June 30, 2013.
- [31] morph-Hom software, <http://cmm.ensmp.fr/morphhom>, accessed June 30, 2013.